Volume 18
Number 37
7 October 2022
Pages 7001–7248

Soft Matter

rsc.li/soft-matter-journal

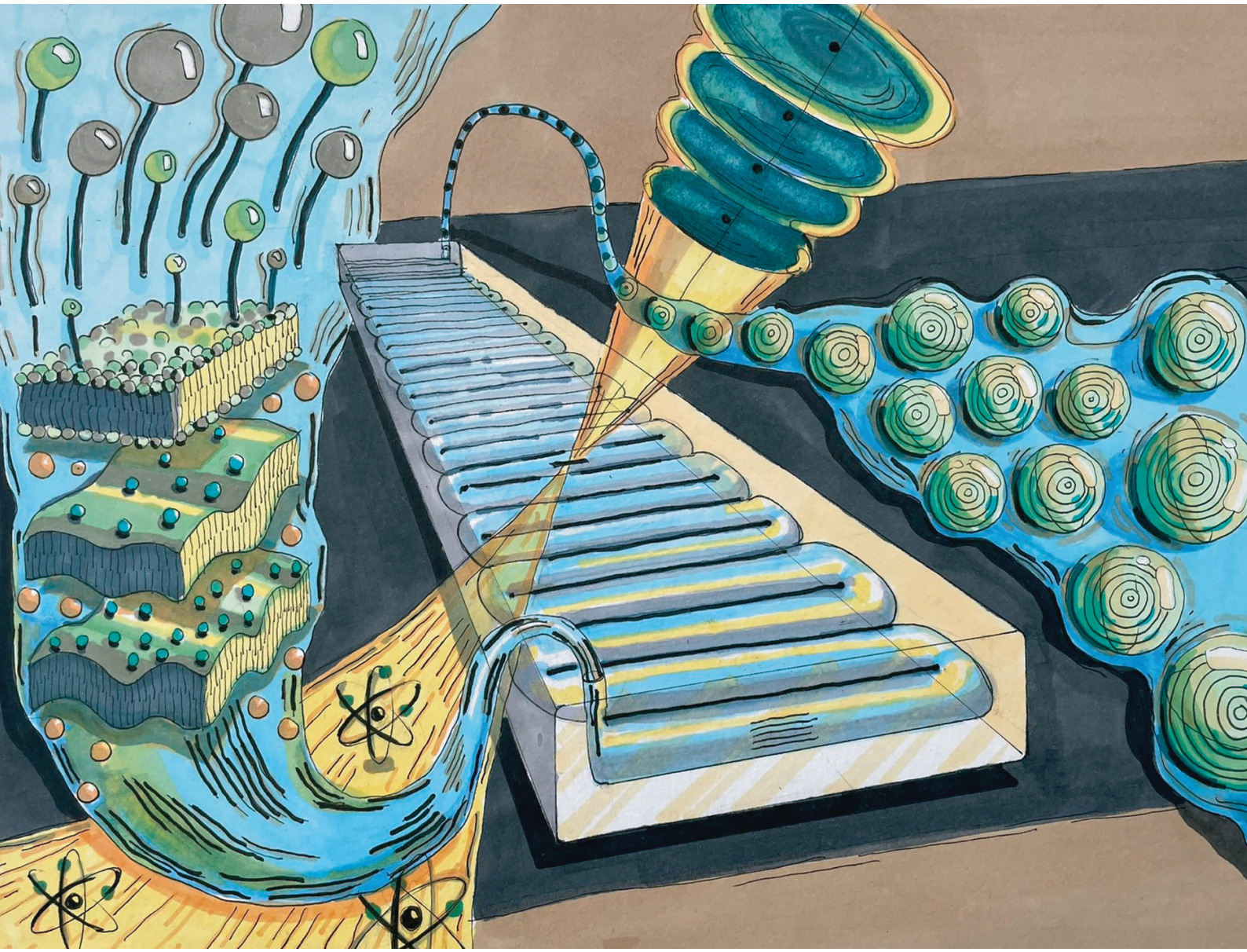

ISSN 1744-6848

ROYAL SOCIETY OF CHEMISTRY

PAPER
João T. Cabral *et al.*
Effect of salt on the lamellar L_α-to-MLV transformation in SDS/octanol/water under microfluidic flow

Soft Matter

PAPER

View Article Online
View Journal | View Issue

Check for updates

Cite this: *Soft Matter*, 2022, **18**, 7010

Effect of salt on the lamellar L_α-to-MLV transformation in SDS/octanol/water under microfluidic flow†

Liva Donina,[a] Lionel Porcar[b] and João T. Cabral *[a]

Received 17th May 2022,
Accepted 23rd July 2022

DOI: 10.1039/d2sm00643j

rsc.li/soft-matter-journal

We investigate the effect of added (NaCl) salt and varying flow rate on the phase behaviour and flow response of a model surfactant L_α phase, sodium dodecyl sulfate (SDS)/octanol/water, using small angle neutron scattering (SANS) and polarised optical microscopy in microfluidics, supported by NMR, viscosity, conductivity and zeta potential measurements. A long (~3 m) tubular microchannel device is employed to quantify the spatiotemporal structural evolution of the system towards multilamellar vesicles (MLV). The effect of salt is rationalised in terms of changes in membrane bending rigidity and phase stability. It is shown that ~1.8 w/w% NaCl addition results in MLV formation within the shortest time (or equivalent lengthscale) and yields near-centrosymmetric scattering profiles characteristic of MLVs (at a reference 1 mL h^{-1} flow rate and ≃90 s^{-1} shear rate). Further salt addition yields biphasic systems that remain strongly aligned under flow, while lower salt content also increases scattering anisotropy, accompanied by higher membrane rigidity and solution viscosity. Increasing flow rate causes greater initial L_α alignment, and thus flow anisotropy, but also faster evolution towards isotropy and MLV formation.

Open Access Article. Published on 25 July 2022. Downloaded on 2/23/2026 6:41:10 AM.
This article is licensed under a Creative Commons Attribution 3.0 Unported Licence.

1 Introduction

Amphiphilic membranes are formed *via* the noncovalent self-assembly of amphiphilic molecules, such as lipids, surfactants, or block-copolymers, into broadly planar monomolecular arrays of one or two layers, characteristic of cell membrane bilayers, and liquid crystalline surfactant lamellar L_α phases. The elastic properties of L_α membranes, namely their low compressibility and low membrane bending rigidity,[1] largely govern their physical behaviour[2,3] and flow response.[4]

Generally, membrane bending rigidity is estimated by either measuring the associated thermal undulation spectrum, or by deforming the membrane and measuring its response, thus involving distinct experimental techniques and data analysis models.[5] Experiments probing individual membranes are generally based on giant unilamellar vesicles (~100 μm), observable by light microscopy, employing fluctuation spectroscopy[6] or micropipette aspiration.[7] Scattering and NMR techniques generally probe concentrated membrane ensembles, or stacks, where neighbouring interactions are important.[1] The membrane bending rigidity is reflected on the line shape of the lamellar Bragg peak measured by small angle neutron or X-ray scattering (SANS, SAXS) which, in a L_α system can be described by the Caillé structure factor $S(q)$ model,[8–10]

$$S(q) \sim (q - q_h)^{1+\eta} \quad (1)$$

where q_h denotes the peak position in reciprocal space, and the Caillé parameter η reads

$$\eta = \frac{\pi k_B T}{2\sqrt{\kappa \bar{B} d^3}} \quad (2)$$

where κ is membrane bending modulus, $\bar{B}$ is membrane compressibility modulus and d corresponds to the L_α repeat distance (d-spacing), k_B is Boltzmann constant and T is temperature. Neutron or X-ray scattering, in conjunction with osmotic stress measurements[11] or dynamic light scattering[12] can determine both κ, and $\bar{B}$. If $\bar{B}$ cannot be measured by ancillary techniques, model estimations can be made, assuming electrostatic or steric interactions between adjacent membranes.[11,13] The inter-membrane potential for charged planes can be obtained from the one-dimensional Poisson–Boltzmann equation, as[13]

$$\bar{B}_{PB} = \frac{\pi k_B T d}{2 l_B (d - \delta)^3} \quad (3)$$

[a] *Department of Chemical Engineering, Imperial College London, London, UK. E-mail: j.cabral@ic.ac.uk; Tel: +44 207 594 5571*
[b] *Institut Laue-Langevin, 71 Avenue des Martyrs, B.P. 156, F-38042 Grenoble Cedex, France*

† Electronic supplementary information (ESI) available. See DOI: https://doi.org/10.1039/d2sm00643j

This journal is © The Royal Society of Chemistry 2022

Open Access Article. Published on 25 July 2022. Downloaded on 2/23/2026 6:41:10 AM.
This article is licensed under a Creative Commons Attribution 3.0 Unported Licence.

where $l_B = e^2/(4\pi\varepsilon_0\varepsilon_r k_B T)$ is the Bjerrum length of the solvent and corresponds to $\simeq 0.7$ nm for water at room temperature and δ is membrane thickness. This theory applies to weakly screened electrostatic repulsions and $\bar{B}_{PB}$ can be decreased by attractive contributions of counterions near the membrane.[14] Steric repulsions can also contribute to the overall $\bar{B}$, as described by Helfrich equation:[15]

$$\bar{B}_{und} = \frac{9\pi^2(k_B T)^2}{64\kappa}\frac{d}{(d-\delta)^4} \quad (4)$$

where κ is membrane bending rigidity and will be relevant for adjacent undulating flexible membranes relevant for d-spacing values below $\simeq 10$ nm.[14]

Experimentally, Neutron Spin Echo (NSE) can measure shape fluctuations in L_α membranes *via* the intermediate scattering function $I(q, t)$ from which κ can be directly estimated,[13,16] although measurements are long ($\sim$days), require large sample volumes ($\sim$several mL), and experimental access is somewhat limited.[1]

The elastic properties of membranes can be modulated by the addition of dopants that embed within the bilayer (*e.g.*, polymers, surfactants, alcohols, nanoparticles) or by addition of salt, thereby impacting κ. As an example, Meklesh and Kekicheff reported that addition of polyethylene glycol (PEG) to sodium dodecyl sulfate(SDS)/octanol/brine system increases membrane bending rigidity once the polymer concentration crossover from dilute to semidilute regimes is reached.[14] The addition of charged surfactants has been found to both increase and decrease L_α membrane bending rigidity.[17,18]

Similarly, addition of salt will impact membrane bending rigidity κ in a manner that will depend on the initial membrane charge. In the case of non-ionic surfactant L_α phases, addition of salt will lead to increase in κ. For example, NaCl addition to nonionic dioleoylphosphatidylcholine (DOPC) L_α phase was reported to increase bending rigidity.[19] In a different study, nonionic $C_{15}E_5$, upon addition of antagonistic $RbBPh_4$ salt, was also found to increase membrane bending rigidity.[13] However, other studies have indicated a decrease in κ with salt addition; for instance, the addition of NaCl to anionic dipalmitoylphosphatidyl glycerol (DDPG) surfactant has been shown to decreased membrane bending rigidity κ, interpreted as due to charge screening of steric repulsions.[20]

In this paper, we consider the impact of salt addition, and thus varying membrane bending rigidity, on the flow-induced transformation of a model L_α surfactant phase into multilamellar vesicles (MLVs). This L_α to MLV transformation[21] has been extensively studied using different shear fields, stress and rates, using various model systems (non-ionic,[22–24] cationic[25,26] and anionic[27,28]) alongside the effect of added co-surfactants[18,29] and salt.[13,19] Zilman and Granek[4] have proposed a theoretical model that estimates the critical shear required for the transformation in terms of the membrane properties (d and κ) and flow geometry, although experimental evidence appears unclear, with increasing membrane bending rigidity resulting in both higher[13,30] or lower critical shear rates.[31]

To date, only a few studies have examined the coupling between L_α membrane elastic properties and their flow response.[13,30,31] Here, we consider the effect of varying NaCl content on the model anionic SDS/octanol/water system in the L_α phase, building upon previous work on the flow-induced MLV phase transformation of the 2% NaCl system investigated by rheometry[28,32–34] and microfluidics.[35,36] We first report on the effect of NaCl under quiescent conditions using SANS, viscometry and electrophoretic measurements (conductivity and zeta potential) to quantify and distinguish the effect of charge to the membrane elastic properties. We then investigate the spatiotemporal evolution of the fluid structure employing microfluidic-SANS,[37] crosspolarised optical microscopy and ^{2}H NMR, and seek to rationalise the behaviour in terms of the L_α membrane properties. We consider both the effect of varying NaCl at a constant flow rate, and the effect of varying flow rate for a select NaCl concentration, and contrast the findings with our previous observations[36] under oscillatory microfluidic flow.

2 Methods

2.1 Sample preparation

Following phase mapping by optical microscopy (Fig. S1, ESI†), the selected L_α concentration, namely 6.5% SDS, 7.9% octanol and 85.6% brine, denoted with a red star in Fig. 1, was prepared with varying salt content. First, brine solutions with concentrations of 0, 1, 5, 10, 15, 18, 20, 22 and 25 g L^{-1} NaCl (ACS Reagent, $\geq$99.0%) in D_2O (Sigma-Aldrich, 99.9 atom% D) corresponding to 0, 17, 86, 171, 257, 308, 342, 376 mM and 427 mM were prepared. These concentrations will be denoted as 0, 0.1, 0.5, 1, 1.5, 1.8, 2.0, 2.2, 2.5 w/w% NaCl in the paper

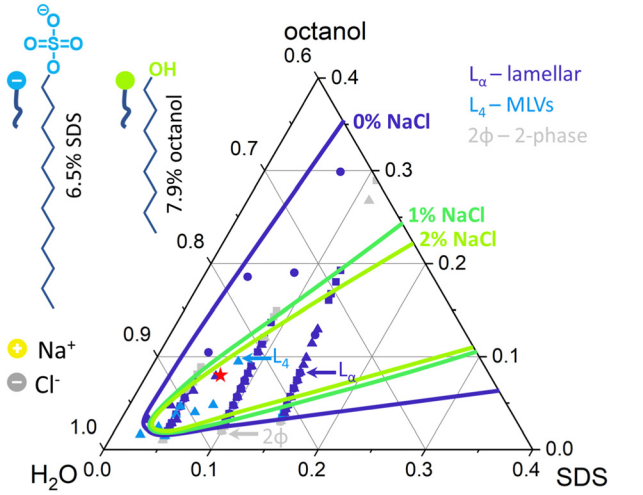

Fig. 1 Ternary phase diagram of SDS/octanol/water system in the presence of NaCl. The (anionic) SDS surfactant molecule is shown in blue, and octanol in green. The coloured lines indicate the phase boundary between the micellar L_1 region and the enclosed L_α regions at selected NaCl concentrations (○) 0, (■) 1%, and (Δ) 2% w/w; selected L_4 (MLV) and two-phase (2ϕ) concentrations are also indicated. The red symbol shows the selected L_α concentration for our study.

Open Access Article. Published on 25 July 2022. Downloaded on 2/23/2026 6:41:10 AM.
This article is licensed under a Creative Commons Attribution 3.0 Unported Licence.

referring to amount of NaCl in brine solution. Following that, 0.65 g (2.25 mmol) of Sodium Dodecyl Sulphate, SDS (Sigma-Aldrich BioXtra, ≥99.0%) were dissolved in 9.52 g (427 mmol) of D_2O brine solution made of 0, 1, 5, 10, 15, 18, 20, 22 and 25 g L^{-1} NaCl. Dissolution was aided by heating to 30 °C until SDS had dissolved and allowed to cool to room temperature. Then, 0.790 g (6.07 mmol) of 1-octanol (Sigma-Aldrich, anhydrous, ≥99%) was added to each of the SDS/brine mixture and stirred for 2 min at 1000 rpm until fully incorporated. The resulting solutions were left to equilibrate for 48 h to mitigate any inadvertent shear effects during sample preparation. The same procedure was employed to prepare samples made for microfluidic experiments but only 1.5%, 1.8%, 2.0% and 2.2% samples were prepared, given their relatively lower viscosity (Fig. S2 (ESI†), 5000–10 000 mPa s) and thus suitability for microfluidic flow.

2.2 Static SANS and data fitting

SANS experiments were performed on the D22 spectrometer at the Institut Laue Langevin, Grenoble. Static measurements used 'banjo' Hellma cells (1 mm path length) with first detector and collimator distance of 5.6 m, second detector distance at 1.4 m and neutron wavelength λ = 6 Å. The measured wavevector q range was 0.01 to 0.8 $Å^{-1}$ and the transmission of the samples was relatively high (>0.8) with low background values of ~0.2 cm^{-1}. The sample rack was kept at room temperature, 25 °C. The data were reduced with GRASP software and data fitting (of radially- and sector-averaged spectra) was performed with SasView 5.0.2, employing the random head-tail sheet with Caillé structure factor model and the fitted parameters compared for the different NaCl concentrations.

2.3 Viscosity measurements

Viscosity shear sweep measurements (Fig. S2, ESI†) were performed using an Anton Paar MCR 302 rheometer equipped with cone plate cell (part no. 79040). Samples investigated were with 0, 0.5, 1.0, 1.5 and 2.0% NaCl concentrations. Each sample was kept at 25 °C, with the gap between the cone-plate set to 0.2 mm and shear sweep performed from 0.1 to 2000 s^{-1} with 20 points per decade, maintaining each shear rate for 20 seconds. The viscosity was measured at low 0.1 s^{-1} shear rate value and high 1000 s^{-1} shear rate.

2.4 Zeta potential and conductivity

Zeta potential and conductivity measurements for micellar SDS/water solutions, and lamellar SDS/octanol/water, were collected using a Litesizer 500 and a Omega cuvette (225288) by injecting 1 mL of sample for every NaCl concentration and rinsing the cuvette in-between runs with DI water. The temperature of the cell was set to 25 °C and the sample was equilibrated for 1 min, after which 3 measurements with 20 runs were performed. The Zeta potential ζ was estimated *via* the Helmholtz–Smoluchowski equation[38] $\zeta = \frac{\mu\eta}{\varepsilon_r\varepsilon_0}$ where μ is the electrophoretic mobility measured experimentally, η is the viscosity of the solution with dielectric constant ε_r and ε_0 is the vacuum permittivity. Conductivity of DI water with various NaCl concentrations was measured with with a Hanna instruments multimeter (HI-2020) equipped with conductivity probe (HI-763100).

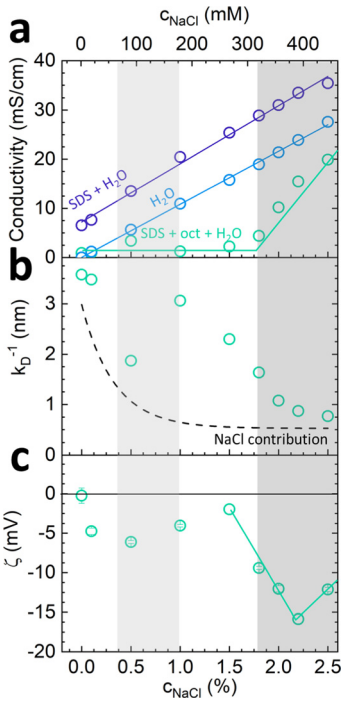

Fig. 2 Conductivity and zeta potential ζ measurements. (a) Conductivity measurements for water, 6.5% SDS/water micellar solution, and 6.5% SDS/7.9% octanol/85.6% water, as a function of NaCl content; (b) Debye length k_D^{-1} estimated by assuming only salt ions contributing to the ionic strength (dashed line) and k_D^{-1} calculated from the experimental conductivity data of SDS/octanol/water/NaCl (circles); the light shaded area indicates a dip in k_D^{-1}, near the 1 : 1 molar ratio of SDS and NaCl (~0.8% NaCl). (c) Zeta potential ζ measurements for SDS/octanol/water system with varying NaCl concentrations estimated from electrophoretic mobility μ_{mob} by the Helmholtz–Smoluchowski equation. The darker shaded area corresponds to the onset of the linear conductivity dependence for the lamellar system with salt addition.

The conductivity of micellar SDS/water and water increases linearly with NaCl at all concentrations investigated, as shown in Fig. 2a. By contrast, the conductivity of the lamellar SDS/octanol/water system remains largely unchanged up to ~1.8–2% NaCl, indicating charge condensation at the membrane surface, and then increasing linearly beyond this threshold, in agreement with the onset of demixing (Fig. 1). This behaviour is qualitatively in line with expectations from Manning theory for counterions condensation on spherical and planar geometries.[39] The Debye length $k_D^{-1} = \sqrt{\frac{\varepsilon_r\varepsilon_0 k_B T}{2ne^2}}$, where n is the number charge density and e is the electric unit charge, was first estimated assuming that only Na^+ and Cl^- ions contribute to number charge density,[13] yielding values between 2.32 and 0.46 nm with increasing NaCl concentration, as shown by the dashed line in Fig. 2b. A more accurate estimate utilises conductivity K_c measurements, as $k_D^{-1} = \sqrt{\frac{\varepsilon_r\varepsilon_0 D}{K_c}}$, where D is

 This journal is © The Royal Society of Chemistry 2022

Open Access Article. Published on 25 July 2022. Downloaded on 2/23/2026 6:41:10 AM.
This article is licensed under a Creative Commons Attribution 3.0 Unported Licence.

diffusion constant for Na^+ and Cl^- ions, D = 1.7 μm^2 ms^{-1},[40] shown as markers. The dip around 0.5–1% NaCl (shaded) coincides with the isoelectric point for this system. Zeta potential measurements are shown in Fig. 2c, approximately following the results of Fig. 2a and b. Specifically, ζ decreases around 1.8–2% NaCl, beyond which the system demixes.

2.5 Serpentine channel microfluidic setup

A commercially available serpentine, ~3 m long, tubular microfluidic device etched in high optical and neutron transmittance crown glass[35,41,42] (Dolomite Microfluidics, ref. 3000281) was selected for these experiments. The device was fitted with a 30 cm long inlet and outlet polytetrafluoroethylene (PTFE) tubing (Cole Parmer, ref. WZ-06406-60, i.d. = 0.79 mm). The sample was slowly poured onto the barrel of a 20 mL stainless steel syringe, and mounted on a high-pressure PHD ULTRA 4400 syringe pump (both Harvard Apparatus). The extremity of the long serpentine channel outlet was connected to the syringe (input); two of three access ports were closed and the remaining one was used as outlet and connected to a waste container. The sample was infused for 60 min to reach a steady state at 0.5–5 mL h^{-1} equivalent to 1.6–16 mm s^{-1} and wall shear rates of ~40–400 s^{-1} (estimated following[43] as $\dot{\gamma} = (4Q/\pi R_{eq}^3)$, where Q is volumetric flow rate and R_{eq} is the equivalent radius of an ellipsoid calculated as $2A/P$ with A is the cross-sectional area, 0.086 mm^2, and P the perimeter, 1.08 mm). Oscillatory rheology data for the 2% NaCl reference system[44] indicate a G' and G'' crossover at ~0.45 s^{-1} corresponding to characteristic timescales of ~2 s. The flow conditions examined can thus be considered 'strong', and well within the shear regime expected for MLV formation.[32] Measurements were recorded for every channel section with optical microscopy and every 7th channel section for SANS. The position of the fluid on the microfluidic chip was calculated inlet length + serpentine channel section number × 24 mm (*i.e.*, the length of each section). Flow profiles obtained by PIV of the fluid in the serpentine channel are given in Fig. S3 (ESI†) and showed plug-like flow.

2.6 Microscopy

Following 60 min infusion of the sample onto the chip, the flow was stopped and microscopy images were then acquired with Olympus BX41 reflection microscope equipped with cross-polarised filters (U-AN-2 analyser and U-PO3 polariser). Image capture was done with a Basler acA2000-165um camera controlled with PylonViewer using 10×/0.25 Ach and 50×/0.50 MPlanFLN Olympus objectives under 10 000 μs and 200 000 μs exposure time respectively. Data were analysed with ImageJ by measuring the average light intensity and FFT for images acquired along the serpentine channel.

2.7 Microfluidic-SANS

The microfluidic chip was mounted on a micromachined aluminium frame, thermalised to 25 °C, on the D22 spectrometer configured as described above. A neutron beam slit mask with dimensions 1.4 cm × 200 μm was used to define the beam footprint, within the bounds of the microdevice dimensions, resulting in a scattering volume of 0.7 μL (given the 0.25 mm sample pathlength, *i.e.* channel depth). The device was illuminated in the neutral flow direction (z in Fig. 3a), probing the xy plane. The channel was aligned with the neutron beam by iteratively scanning the empty chip and tracking the scattering and transmission signals along x and y directions until a microchannel map is resolved. Continuous microfluidic experiment was performed for 4 different NaCl concentrations (1.5, 1.8, 2.0 and 2.2%) scanning every 7th channel section, as shown in Fig. 3b. As above, the data were reduced with GRASP, sector averaged, and fitted with SasView 5.0.2 employing the random head-tail sheet with Caillé structure factor model.

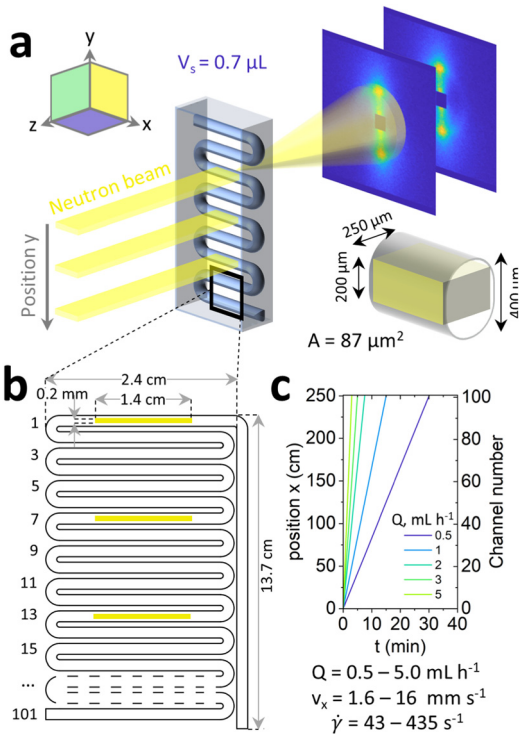

Fig. 3 SANS microfluidic setup and experimental parameters. (a) Serpentine microchannel device illuminated, channel by channel, along the y-direction, under steady state flow conditions (0.5–5.0 mL h^{-1}). The channel dimensions are indicated, and the neutron beam slit is illustrated in yellow. (b) Microchannel dimensions and arrangement; the beam slit defines a horizontal length and vertical height of 1.4 cm × 200 μm and, for a channel depth of 250 μm, resulting in an illuminated volume $V_s \simeq 0.7$ μL. (c) Sample position, and corresponding serpentine channel number, as a function of time for 0.5, 1.0, 2.0, 3.0 and 5.0 mL h^{-1} flow rates indicated in legend, corresponding to average linear velocity v_x range of 1.6–16 mm s^{-1} and estimated wall shear rate range 43–435 s^{-1}.

3 Results

3.1 The effect of salt on the L_α phase

The effect of salt on the L_α phase was initially investigated under quiescent conditions with optical microscopy (Fig. 1, an Fig. S1, ESI†) and SANS. 2D scattering images (Fig. 4a, for front and rear detectors) show higher order diffraction orders for 0% NaCl that gradually disappear with increasing NaCl concentrations.

Open Access Article. Published on 25 July 2022. Downloaded on 2/23/2026 6:41:10 AM.
This article is licensed under a Creative Commons Attribution 3.0 Unported Licence.

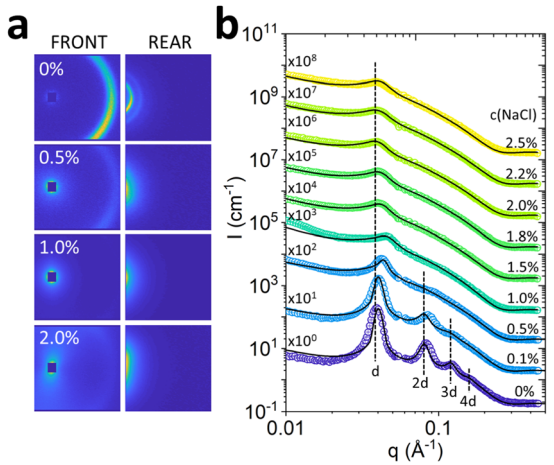

Fig. 4 SANS data at quiescent conditions. (a) 2D scattering profiles for selected NaCl concentrations (0%, 0.5%, 1.00%, 2.0% w/w) acquired simultaneously in two detectors, indicated as 'front' (distance 5.6 m) and 'rear' (distance 1.3 m) detectors. (b) Radially-averaged $I(q)$ profiles for SDS/octanol/brine 6.5%/7.9%/85.6% with NaCl concentrations in brine ranging from 0–2.5% w/w. The dashed vertical lines indicate peak positions corresponding to d, $2d$, $3d$ and $4d$ ($q^* \simeq 0.04$, 0.08, 0.12, 0.16 Å^{-1}), denoting the primary, secondary, tertiary and quaternary Bragg peaks, whose equidistant spacing between indicates L_α stacks. Deviation from the dashed line are discussed in the text. The profiles are shifted vertically for clarity by the multiplicative factors shown.

The radially-averaged scattering profiles $I(q)$ exhibit equidistant Bragg peaks ($q^* \simeq 0.04$ Å^{-1}, $2q^* \simeq 0.08$ Å^{-1}, $3q^* \simeq 0.12$ Å^{-1} and $4q \simeq 0.16$ Å^{-1}) indicating the presence of bilayer structures characteristic of L_α phases (Fig. 4b). The higher order features[45] can be disturbed by fluctuations of the L_α sheets.[46,47] Indeed, we observe a decrease in membrane ordering, indicated by the disappearance of secondary, tertiary and quaternary Bragg peaks upon the addition of NaCl (Fig. 4b). The decrease in L_α ordering was accompanied by a decrease in low shear rate (0.1 s^{-1}) viscosity, which follows a linear trend up to 1.0% NaCl addition, and then largely remains unchanged at higher salt (detailed in Fig. S2b, ESI†).

The $I(q)$ profiles were fitted with the Caillé structure factor model, shown by the solid lines in Fig. 4b, and detailed in Fig. S4–S6 (ESI†). The Caillé parameter η was found to increase rapidly with the addition of NaCl, as shown in Fig. 5a, reaching a plateau of 1, which is the limit of the model assumptions. The solid line is an exponential rise to maximum, employed as a guide to the eye. An approximate d-spacing of 150 Å was observed across all NaCl concentrations, although varying from 156 Å at 0% NaCl, and dropping to 135 nm at 1%, near the 1 : 1 molar ratio of SDS : NaCl. The bilayer thickness δ was calculated as $2(l_{tail} + l_{head})$ remains largely unchanged upon the addition of NaCl (Fig. 5a) indicating no appreciable swelling.

From the fitted η values and eqn (2), $\bar{B}\kappa$ was estimated and found to decrease monotonically with increasing NaCl concentration, as shown in Fig. 5b. Theoretical $\bar{B}$ estimates were obtained by eqn (3) assuming only electrostatic contributions, and are plotted in Fig. 5c (including steric contributions shown in Fig. S7, ESI†). These indicate a non-monotonic behaviour

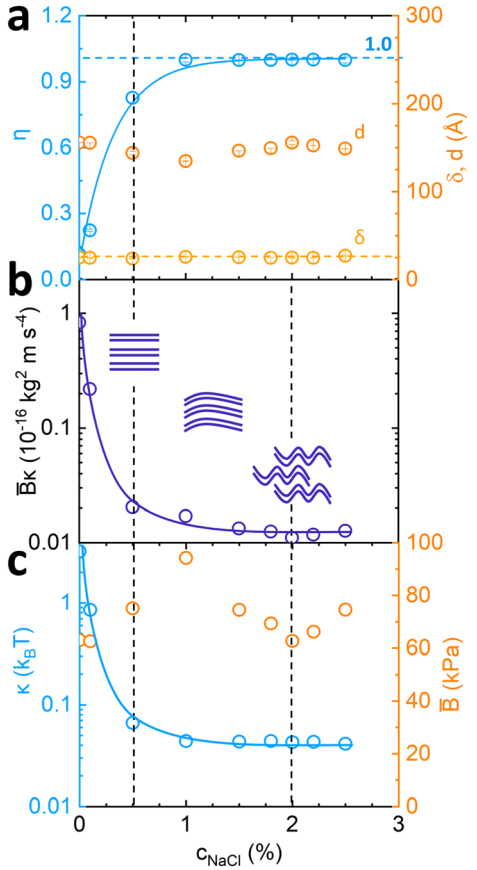

Fig. 5 Fitted parameters from Fig. 2 according to the Caillé structure factor model. (a) Caillé parameter η and L_α spacing d dependence on NaCl concentration; (b) estimated $\bar{B}\kappa$ value dependence on NaCl concentration, where $\bar{B}$ is the compressibility modulus and κ is membrane bending rigidity, and accompanying schematics; (c) calculated $\bar{B}$ values from $\bar{B}_{PB} = \frac{\pi k_B T d}{2 l_B (d-\delta)^3}$ and corresponding κ from $\bar{B}\kappa$ model fit estimates.

upon addition of NaCl with highest value of 95 kPa when SDS : NaCl molar ratio is 1 : 1 (c(NaCl) = 1%) and subsequent drop in value until phase transition boundary conditions are reached around 2% NaCl (Fig. 5c). The membrane sheet schematics illustrate the decrease in stiffness and long range order induced by the salt addition. Parameter κ was estimated from model fitting results and theoretical $\bar{B}$ calculations indicating an overall decrease in membrane bending rigidity (Fig. 5c) from 3.2 k_BT to 0.04 k_BT. This decreasing trend is consistent with that of the Debye length k_D^{-1} (shown in Fig. 2b) indicating $k_D^{-1} \simeq$ 3.58 nm at low NaCl concentrations, decreasing to $\simeq$0.78 nm at high NaCl, thus corresponding to approximately 1/4 to 1/20 of the lamellar d-spacing. A previous study of salt addition to dipalmitoylphosphatidylglycerol (DPPG)[20] also reported a decrease in k_D^{-1} with decreasing κ, as expected for reduced electrostatic repulsions.

3.2 Effect of NaCl on the lamellar phase under continuous microfluidic flow (fixed flow rate)

The effect of NaCl addition on the flow response of the L_α phase under continuous microfluidic flow was examined by a

This journal is © The Royal Society of Chemistry 2022

Open Access Article. Published on 25 July 2022. Downloaded on 2/23/2026 6:41:10 AM.
This article is licensed under a Creative Commons Attribution 3.0 Unported Licence.

combination of crosspolarised optical microscopy, ^{2}H NMR and SANS. At a fixed flow rate of 1 mL h^{-1}, the residence time of the fluid within the microchannel length probed was ~12 min. In general, the correspondence between position, channel section, and residence time for different flow rates is illustrated in Fig. 3c. Given the higher viscosities of low NaCl systems, the following concentrations were selected for microfluidic experiments at fixed flow rate of 1 mL h^{-1}: 1.5, 1.8, 2.0 and 2.2% NaCl, in order to ensure the safe operation of the microdevice within a pressure operating range below 30 bar. (Pressure drop estimations are shown in Fig. S3c (ESI†), based on the Hagen–Poiseuille equation $\Delta p = 8\pi\mu LQ/A^2$ where L is the channel length, Q is the volumetric flow rate, μ is dynamic viscosity and A the cross-sectional area of the channel). The system was allowed to equilibrate for ~1 h, greatly exceeding the residence time of ~12 min (at 1 mL h^{-1}), at an average flow velocity ~3.21 mm s^{-1}. The corresponding wall shear rate is estimated[43] at ≃87 s^{-1}, within the regime in which L_α-to-MLV transformation was previously observed.[32,48,49]

Optical birefringence measurements at the centre of each serpentine channel section (2.4 cm length) showed a decrease in (crosspolarised) light intensity along microchannel position, as shown in Fig. 6a, for NaCl concentrations between 1.5–2%, beyond which (2.2% NaCl) the trend is reversed. Given that light intensity scales approximately with feature size, the results suggest a size decrease and ordering of the characteristic fluid structures. Complementary ^{2}H NMR data were acquired at reference start (*) and end (**) positions, illustrated for 1.8% and 2.2% NaCl in Fig. 6b. The single peak observed at 1.8% is characteristic of an isotropic fluid, contrasting with the dual peaks of 2.2%, expected for an anisotropic fluid. We thus expect the former to correspond to MLVs and the latter to an oriented lamellar sheet structure. Further the end-channel (**) data of 1.8% NaCl shows a narrowing of the peak upon microflow, expected for increasing uniformity in MLV size.

Optical images acquired at the channel entrance and at position 210 cm are indicated with * and ** in Fig. 6c, corroborating a varying degree of ordering amongst the 1.5–2.2% NaCl samples. A fine, regular texture is observed for the resulting fluid structure (**) for 1.8 and 2.0% NaCl, accompanied by FFTs exhibiting a cloverleaf pattern. Structures observed at the bends of the serpentine channel sections, shown in Fig. 6d, were of higher overall average light intensity, reflecting the additional rotational component of the shear flow. Overall, while the light intensity and MLV texture dimensions decrease along the microchannel position, these do not reach a plateau, indicating that a morphology of regularly packed onions is not attained within the experimental timescales. Employing oscillatory flow and contraction-expansion flows, enabling longer residence times of ~2 h, we have previously observed an asymptotic optical characteristics after approximately 60 min shearing times at similar shear rate regime.[36]

In order to resolve the nanoscale arrangement of the L_α structure, we employed microfluidic-SANS and a narrow, rectangular, beam slit (1.4 cm × 200 μm) precisely aligned along the horizontal channel sections, as shown in Fig. 3b,

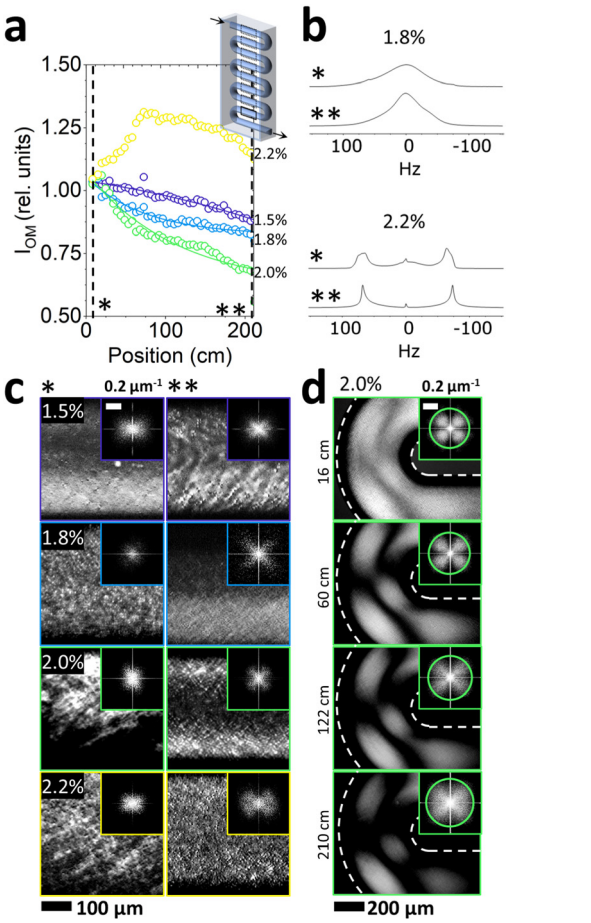

Fig. 6 Measured polarised optical microscopy light intensity and texture evolution as a function of channel position. (a) Relative intensity (referenced to the start position) for NaCl concentrations of 1.5, 1.8. 2.0 and 2.2% w/w; (b) ^{2}H NMR of 1.8 and 2.2% NaCl showing the sample before (top) and after (bottom) being subjected to microfluidic flow; (c) optical textures and FFTs at 'start' (14.9 cm) and ('end') position 211 cm, corresponding to 11 min shear time; (d) optical texture and FFTs at bends along the channel at positions of 16, 60, 122, 210 cm for 2.0% NaCl.

illuminating a 0.7 μL sample volume. Given the low illuminated volume (0.7 μL), each SANS spectrum was recorded for 20 min to acquire adequate statistics. The centre of every 7th channel section, along the y direction, was sampled, corresponding to 17 channel positions along the serpentine channel, as illustrated in Fig. 5b.

The scattering data at the start of the microchannel are generally anisotropic, as expected for aligned L_α sheets, for all NaCl concentrations. Sector analysis of $I(q)$ reveals greater alignment along the normal (xz) direction to flow, than along the flow direction, illustrated in Fig. 7a for channel position 15 cm. The scattering varies non-monotonically with NaCl content and is lowest, and least anisotropic for 1.8% NaCl; at the highest NaCl concentration investigated, 2.2%, the anisotropy is greatest and no scattering peak is visible along the flow direction (xz). This behaviour is expected for MLVs at 1.8% and sheets a 2.2% NaCl.

Further analysis of the evolution of the alignment along the chip was carried out by integrating the scattering intensity

Open Access Article. Published on 25 July 2022. Downloaded on 2/23/2026 6:41:10 AM.
This article is licensed under a Creative Commons Attribution 3.0 Unported Licence.

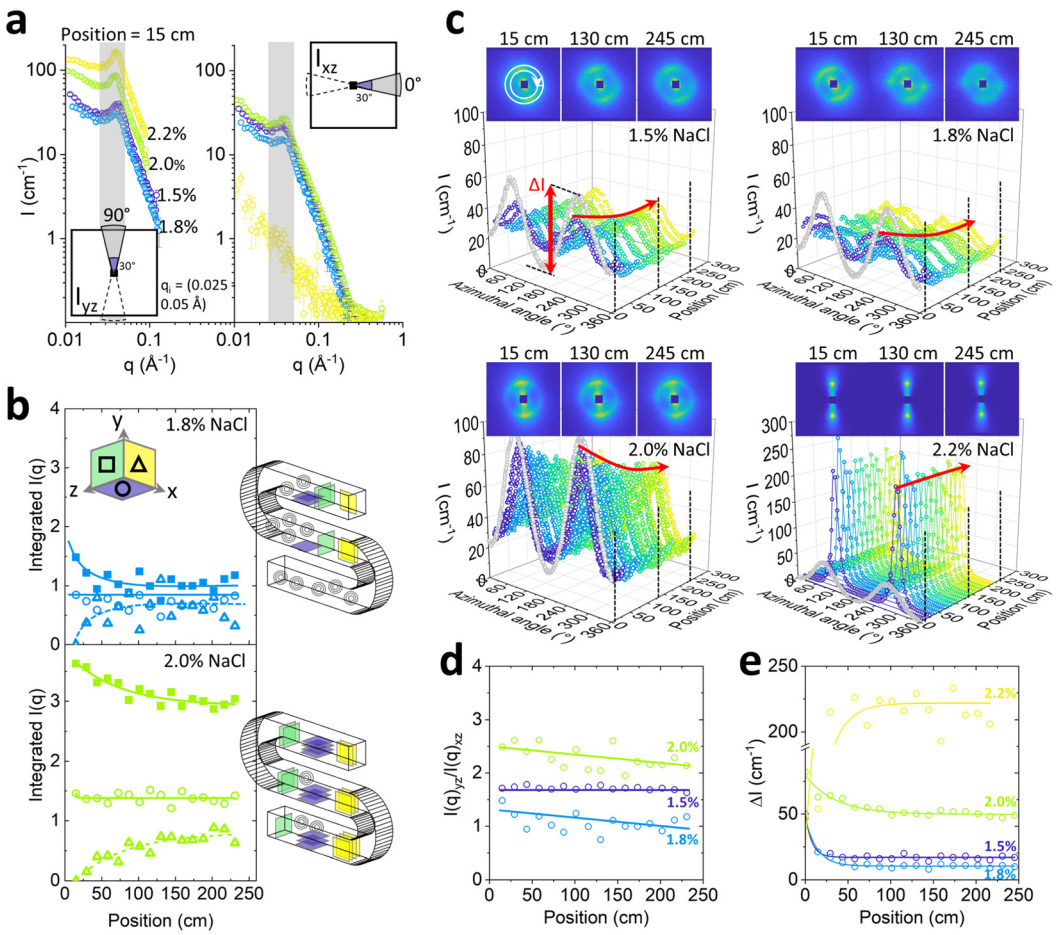

Fig. 7 Effect of salt on the SANS flow evolution of the lamellar phase on serpentine microfluidic chip at fixed flow rate of 1 mL h^{-1}. (a) Sector analysis at 90° and 0° (with 30° angular integration range) probing lamellar sheets aligned, respectively, with the flow (along the *xz* plane) and perpendicularly to the flow (along the *yz* plane); (b) integrated scattering intensity at the Bragg peak ($0.025 \leq q \leq 0.05$ $Å^{-1}$) as a function of channel position for *yz* (■), *xz* planes (○) and inferred for *xy* plane (Δ), shown as dashed line, for 1.8% NaCl (top) and 2.0% NaCl (bottom). Schematics illustrate the transformations inferred; (c) azimuthal averages of 2D SANS scattering patterns as a function of channel position, computed within $0.035 \leq q \leq 0.045$ $Å^{-1}$, for 1.5, 1.8, 2.0 and 2.2% NaCl. Selected 2D patterns at channel positions 15 cm, 130 cm and 245 cm are indicated on the left, and by the vertical dashed lines. A degree of anisotropy ΔI is computed from $I_{max} - I_{min}$ in the azimuthal plots, hence $\Delta I \rightarrow 0$ corresponding to an isotropic pattern; (d) comparison between populations of lamellar sheets aligned with the flow and perpendicular to the flow; (e) SANS ΔI computed as a function of the serpentine channel position for the various NaCl concentrations; lines are guides to the eye.

under the Bragg peak (within $0.025 \leq q \leq 0.05$ $Å^{-1}$) as a function of channel position, as shown in Fig. 7b for 1.8% and 2.0% NaCl. The integrated intensity along the flow *xz*, and perpendicularly to the flow *yz*, is shown by ○ and Δ markers respectively. The relative fraction of sheets on *xy* plane cannot be measured directly, but its evolution along channel position was estimated by subtracting the sum of intensities on the *yz* and *xz* planes and subtracting their initial value, *i.e.* at the start of the channel. In this way, assuming that the overall scattering integral remains approximately constant within this *q*-range, the intensity in the 'missing plane' corresponding to the fraction of sheets exchanged into *xy* plane can be inferred, indicated by ΔI_{xy} in terms of intensity. In the case of 1.8%, the relative sheet alignment approaches a similar end point, implying that the populations of the sheets in all principal directions are approximately equal, and this isotropic structure supports the formation of MLVs. The alignment observed for 2.0% NaCl is evidently not equal at this channel position, but gradually evolves to become more isotropic along the channel, compatible with partial MLV formation.

The evolution of the orientational order under flow for each NaCl concentration was further examined by the azimuthal analysis of the 2D scattering spectra, integrated within a narrow *q* range 0.035–0.045 $Å^{-1}$ (Fig. 7c). In the case of 1.5% and 1.8% NaCl, anisotropy decreased rapidly along the channel position, while for 2.0% NaCl, the anisotropy decreases modestly and the lamellar sheets remain largely aligned within the microchannel length (up to ~250 cm) and flow time (~12 min). By contrast, the system with 2.2% NaCl content remains highly aligned throughout, as expected for lamellar sheets under shear flow; from the optical phase mapping data, this concentration corresponds to the onset of demixing.

These results corroborate the sector analysis provided in Fig. 7b, in terms of the absolute peak intensity evolution towards

 This journal is © The Royal Society of Chemistry 2022

Open Access Article. Published on 25 July 2022. Downloaded on 2/23/2026 6:41:10 AM.
This article is licensed under a Creative Commons Attribution 3.0 Unported Licence.

more isotropic structures, in particular for the 1.8% NaCl system. Fig. 7b and c show the ratio between $I(q)_{yz}$ and $I(q)_{xz}$ populations (Fig. 7d) and the maximum amplitude of the azimuthal intensity variation, termed ΔI (Fig. 7e), as a function of channel position. The results are consistent to those reported by optical microscopy in Fig. 6a, albeit the SANS data readily reach a plateau value within relatively short channel travel distances ($\sim$25–100 cm). In terms of NaCl content, the systems can be readily ranked from iso- to anisotropic, as 1.8%, 1.5%, 2.0% and finally 2.2% NaCl. The fact that the SANS data exhibit asymptotic behaviour within short channel distances (and thus times) is expected given the nanoscale dimensions probed, while the larger, micronscale regular arrangements probed by optical microscopy evolve subsequently and refine over much longer times.[36]

3.3 Effect of varying microfluidic flow rate on the lamellar phase (fixed salt content)

We next consider the effect of varying flow magnitude on the L_α-to-MLV transformation by investigating flow rates 0.5, 1.0, 2.0, 3.0 and 5.0 mL h^{-1} with microflow-SANS at a fixed 2.0% NaCl concentration, for consistency with previous work on this system. These flow rates yield wall shear rates estimates of 40–400 s^{-1}, in the range expected for MLV formation for this system (10–1000 s^{-1}),[32] Comparing the integrated area of radially averaged $I(q)$ sectors parallel (xz) and orthogonal (yz) to the flow, shown in Fig. 8a, follows that increasing flow rate has the dual effect of (i) inducing a greater initial lamellar sheet alignment, while also (ii) causing a more rapid decrease in anisotropy subsequently, as shown in Fig. 8b and c. The latter plots the ratio of the integrated sector intensities $I(q)_{yz}/I(q)_{xz}$, which increases approximately linearly with flow rate, and decreases with microchannel position. Direct observation of 2D scattering images, in Fig. 8d, shows that the anisotropic profiles evolve gradually along channel position, and the azimuthal analyses for 0.5, 1.0 and 5.0 mL h^{-1} quantify the decrease in anisotropy at the higher flow rates (1.0 and 5.0 mL h^{-1} shown) but exhibits virtually no change at the lowest rates of 0.5 mL h^{-1} (see Fig. S8 (ESI†) for 2.0 and 3.0 mL h^{-1}). While the flow alignment of the L_α phase is expected and widely reported (*e.g.*, ref. 35 and 50), the subsequent decrease in anisotropy under microfluidic flow indicates a gradual evolution towards MLVs, within the accessible residence time windows. Previous mechanistic

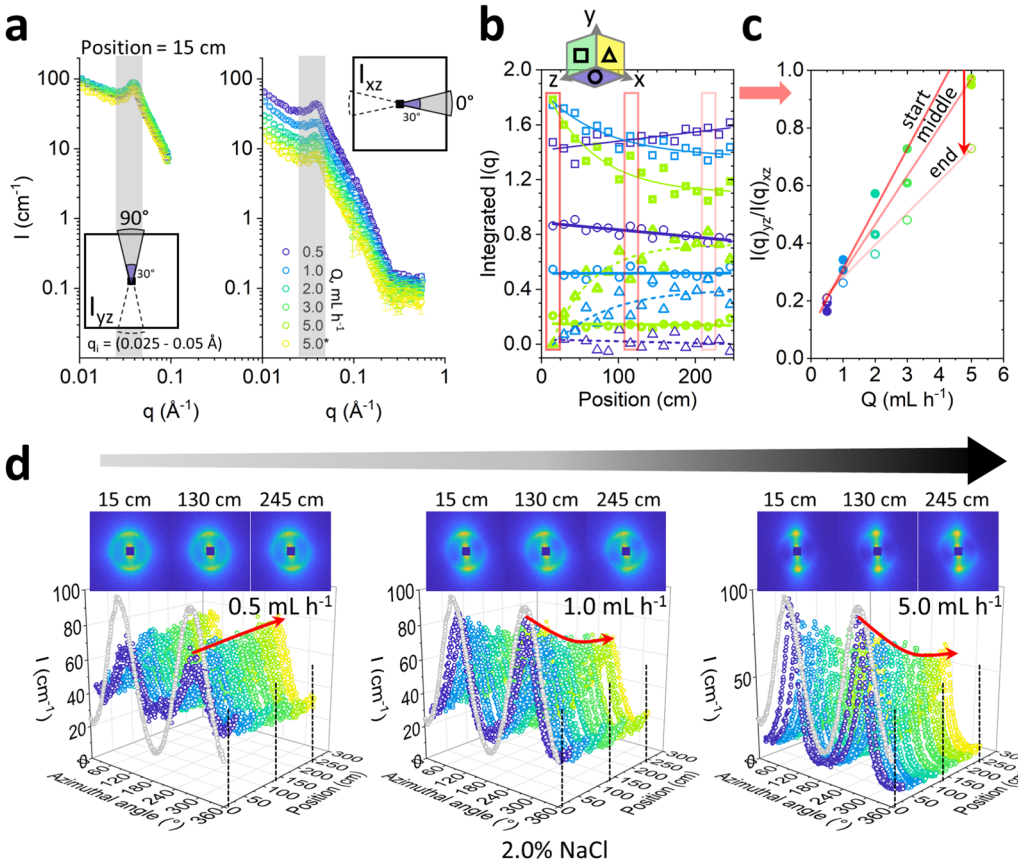

Fig. 8 Effect of flow rate on the lamellar phase at fixed 2.0% NaCl measured by SANS. (a) SANS sector analysis at 90° and 0° (with 30° angular integration range) probing, respectively, lamellae sheets aligned with the flow (along the xz plane), and perpendicularly to the flow (along the yz plane); (b) integrated scattering intensity at the Bragg peak ($0.025 \leq q \leq 0.05$ Å^{-1}) as a function of channel position for yz (■), xz (○) and inferred xy (Δ) planes for flow rates of 0.5, 1 and 5 mL h^{-1}; (c) ratio $I(q)_{yz}/I(q)_{xz}$ of integrated populations reflecting the effect of flow rate (Q = 0.5–5 mL h^{-1}) on the anisotropy (higher value indicating higher anisotropy) for illustratibe channel positions 15, 130 and 245 cm denoted as 'start', 'middle' and 'end' respectively; (d) azimuthal averages of 2D SANS scattering patterns as a function of channel position, computed within $0.035 \leq q \leq 0.045$ Å^{-1}, for 0.5, 1 and 5 mL h^{-1}. Selected 2D patterns at illustrative channel positions indicated by the vertical dashed lines.

Open Access Article. Published on 25 July 2022. Downloaded on 2/23/2026 6:41:10 AM.
This article is licensed under a Creative Commons Attribution 3.0 Unported Licence.

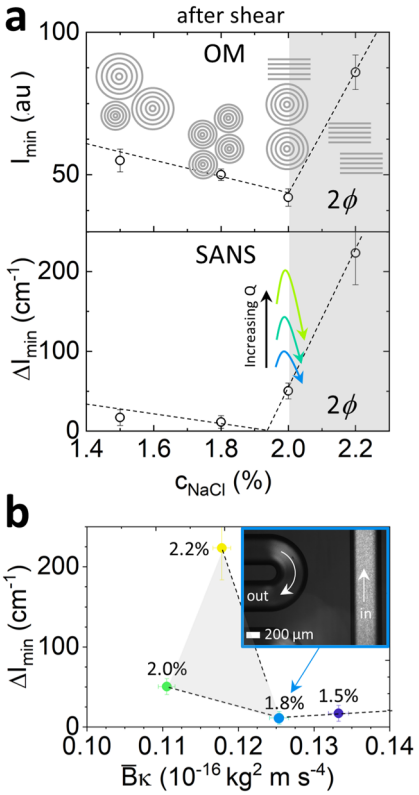

Fig. 9 Optical and SANS intensity dependence on NaCl concentration at a fixed 'end' channel position 245 cm. (a) Optical (top) and SANS azimuthal (bottom) intensity dependence on NaCl concentration and flow rate, with accompanying schematics. The dashed lines are guides to the eye. Qualitative effect of flow rate at a reference 2% NaCl concentration is indicated with arrows; (b) SANS azimuthal intensity ΔI_{min} as a function of $\bar{B}\kappa$ computed from the quiescent data in Fig. 4b.

studies of MLV formation suggest that lamellar sheets first align with the flow and experience a suppression of membrane undulations,[4,51] eventually resulting in vesicle formation at sufficiently high shear rates and longer times.

By contrast, oscillatory flows can potentially facilitate MLV-formation by selecting a different pathway.[22] From a practical viewpoint, oscillatory flow fields also permit a decoupling between flow rate and residence time (which are otherwise constrained as illustrated in Fig. 3c), and thus the investigation of arbitrarily long shearing times. In Fig. S9 (ESI†), we contrast the effect of continuous (this work) and oscillatory[36] flows on the L_α-to-MLV transformation on the same system. Overall, we find that the transformation rate is greater for oscillatory flow under comparable velocity and wall shear rate conditions (Fig. S9d, ESI†), highlighting the role of rotational flow components and acceleration/deceleration often found in practical flow nozzles used in MLV generation by flow processing.

4 Conclusions

We have considered the effect of salt addition (0–2.5% NaCl) on the phase behaviour and microstructure of a model L_α system, namely 6.5% SDS/7.9% octanol/85.6% brine, known to undergo a lamellar-to-MLV transition under flow. Salt addition was found to decrease L_α ordering, increase the Caillé parameter, and correspondingly decrease $\bar{B}\kappa$, the product of membrane compressibility modulus and bending rigidity, while the membrane thickness remained largely unchanged, and the d-spacing varied non-monotonically. The effect of flow was examined using a serpentine microfluidic device, consisting of a $\sim$3 m long tubular microchannel, operated in continuous flow, using polarised optical microscopy and SANS. Owing to operating pressure limits of the microdevice, and the high viscosity of the L_α system, NaCl content $>$1.5% were investigated under flow. Salt addition was found to promote MLV formation up to a crossover point between 1.8 and 2.0% NaCl.

Fig. 9 provides an overview of our findings, in terms of the scattering observables, fitted membrane properties and accompanying lamellar schematics. Fig. 9a shows the terminal (minimum) value I_{min} of the cross-polarised light intensity (top), and the azimuthal intensity amplitude at Bragg peak, ΔI_{min}, measured at the end position measured along the serpentine channel (bottom), as a function of NaCl concentration. At a fixed 2% NaCl addition, we examined the effect of increasing flow rate, which was found to increase the initial alignment of the L_α phase, and thus increase flow anisotropy, but also subsequently cause a faster decrease in anisotropy as a function of time, toward MLV formation. Fig. 9b then correlates ΔI_{min} with the fitted $\bar{B}\kappa$ parameter obtained from quiescent SANS data, exhibiting a minimum value corresponding to the 1.8% NaCl concentration with $\bar{B}\kappa \simeq 0.125 \times 10^{-16}$ kg^2 ms^{-1}; for this system, further decreasing $\bar{B}\kappa$ leads to the onset of demixing, and therefore does not facilitate MLV formation. The apparent inversion of the trend between 2.0 and 2.2% NaCl is likely due to the fact that the latter is within the biphasic region. An optical image taken near the channel inlet and outlet for the 1.8% NaCl concentration is included as inset, illustrating the change in optical texture and intensity effected by the microchannel flow. Our combined microfluidic SANS and optical approach is thus able to relate L_α membrane properties to continuous flow behaviour in a tubular geometry, relevant to most practical flow processing of such fluids, relating MLV formation to the effect of salt, and establishing 1.8% NaCl as an 'optimal' condition for this system.

Conflicts of interest

There are no conflicts to declare.

Acknowledgements

We thank the Institut Laue Langevin (Grenoble) for beamtime; data available on doi.ill.fr/10.5291/ILL-DATA.9-10-1651 (static SANS) and doi.ill.fr/10.5291/ILL-DATA.9-10-1706 (flow SANS). We thank EPSRC and Imperial College London for a PhD studentship for LD. JTC acknowledges the Royal Academy of Engineering (RAEng, UK) and Procter & Gamble for funding a Research chair.

This journal is © The Royal Society of Chemistry 2022

Open Access Article. Published on 25 July 2022. Downloaded on 2/23/2026 6:41:10 AM.
This article is licensed under a Creative Commons Attribution 3.0 Unported Licence.

References

1 R. Dimova, *Adv. Colloid Interface Sci.*, 2014, **208**, 225–234.
2 M. Gradzielski, *Curr. Opin. Colloid Interface Sci.*, 1998, **3**, 478–484.
3 D. Andelman, *Handb. Biol. Phys.*, 1995, **1**, 603–642.
4 A. Zilman and R. Granek, *Eur. Phys. J. B*, 1999, **11**, 593–608.
5 D. Bochicchio and L. Monticelli, *Adv. Biomembr. Lipid Self-Assem.*, 2016, **23**, 117–143.
6 A. C. Rowat, P. L. Hansen and J. H. Ipsen, *Europhys. Lett.*, 2004, **67**, 144–149.
7 G. H. Sagar and J. R. Bellare, *J. Phys. Chem. B*, 2009, **113**, 13805–13810.
8 D. Roux and C. Safinya, *J. Phys.*, 1988, **49**, 307–318.
9 F. Nallet, R. Laversanne and D. Roux, *J. Phys. II Fr.*, 1993, **3**, 487–502.
10 R. Zhang, S. Tristram-Nagle, W. Sun, R. L. Headrick, T. C. Irving, R. M. Suter and J. F. Nagle, *Biophys. J.*, 1996, **70**, 349–357.
11 G. Brotons, M. Dubois, L. Belloni, I. Grillo, T. Narayanan and T. Zemb, *J. Chem. Phys.*, 2005, **123**, 1–18.
12 M.-F. Ficheux, A.-M. Bellocq and F. Nallet, *J. Phys. II*, 1995, **5**, 823–834.
13 Y. Kawabata, R. Bradbury, S. Kugizaki, K. Weigandt, Y. B. Melnichenko, K. Sadakane, N. L. Yamada, H. Endo, M. Nagao and H. Seto, *J. Chem. Phys.*, 2017, **147**, 034905.
14 V. Meklesh and P. Kékicheff, *J. Colloid Interface Sci.*, 2021, **582**, 1158–1178.
15 W. Helfrich, *Z. Naturforsch.*, 1973, **28**, 693–703.
16 M. Mell, L. H. Moleiro, Y. Hertle, P. Fouquet, R. Schweins, I. López-Montero, T. Hellweg and F. Monroy, *Eur. Phys. J. E: Soft Matter Biol. Phys.*, 2013, **36**, 75.
17 R. Bradbury and M. Nagao, *Soft Matter*, 2016, **12**, 9383–9390.
18 H. Egger, G. H. Findenegg, O. Holderer, R. Biehl, M. Monkenbusch and T. Hellweg, *Soft Matter*, 2014, **10**, 6926–6930.
19 J. U. De Mel, S. Gupta, R. M. Perera, L. Ngo, P. Zolnierczuk, M. Bleuel, S. V. Pingali and G. J. Schneider, *Langmuir*, 2020, **36**, 9356–9367.
20 B. S. Lu, S. P. Gupta, M. Belicka, R. Podgornik and G. Pabst, *Langmuir*, 2016, **32**, 13546–13555.
21 O. Diat and D. Roux, *J. Phys. II*, 1993, **3**, 9–14.
22 S. Kuczera, L. Gentile, T. I. Brox, U. Olsson, C. Schmidt and P. Galvosas, *Langmuir*, 2018, **34**, 8314–8325.
23 L. Gentile, M. A. Behrens, S. Balog, K. Mortensen, G. A. Ranieri and U. Olsson, *J. Phys. Chem. B*, 2014, **118**, 3622–3629.
24 Y. Kosaka, M. Ito, Y. Kawabata and T. Kato, *Langmuir*, 2010, **26**, 3835–3842.
25 Z. Yuan, S. Dong, W. Liu and J. Hao, *Langmuir*, 2009, **25**, 8974–8981.
26 C. Liu and J. Hao, *J. Phys. Chem. B*, 2011, **115**, 980–989.
27 L. Coppola, L. Gentile, I. Nicotera, C. O. Rossi and G. A. Ranieri, *Langmuir*, 2010, **26**, 19060–19065.
28 A. S. Wunenburger, A. Colin, J. Leng, A. Arnéodo and D. Roux, *Phys. Rev. Lett.*, 2001, **86**, 1374–1377.
29 C. R. Safinya, D. Roux, G. S. Smith, S. K. Sinha, P. Dimon, N. A. Clark and A. M. Bellocq, *Phys. Rev. Lett.*, 1986, **57**, 2718–2721.
30 S. Fujii, D. Mitsumasu, Y. Isono and W. Richtering, *Soft Matter*, 2012, **8**, 5381–5390.
31 A. Léon, D. Bonn, J. Meunier, A. Al-Kahwaji, O. Greffier and H. Kellay, *Phys. Rev. Lett.*, 2000, **84**, 1335–1338.
32 P. Sierro and D. Roux, *Phys. Rev. Lett.*, 1997, **78**, 1496–1499.
33 J. B. Salmon, A. Colin and D. Roux, *Phys. Rev. E: Stat., Nonlinear, Soft Matter Phys.*, 2002, **66**, 1–13.
34 Z. Yatabe, R. Hidema, C. Hashimoto, R. B. Pansu and H. Ushiki, *Chem. Phys. Lett.*, 2009, **475**, 101–104.
35 C. G. Lopez, T. Watanabe, A. Martel, L. Porcar and J. T. Cabral, *Sci. Rep.*, 2015, **5**, 1–7.
36 L. Donina, A. Rafique, S. Khodaparast, L. Porcar and J. T. Cabral, *Soft Matter*, 2021, **17**, 10053–10062.
37 C. G. Lopez, T. Watanabe, M. Adamo, A. Martel, L. Porcar and J. T. Cabral, *J. Appl. Crystallogr.*, 2018, **51**, 570–583.
38 Z. Ge and Y. Wang, *J. Phys. Chem. B*, 2017, **121**, 3394–3402.
39 G. S. Manning, *J. Phys. Chem. B*, 2007, **111**, 8554–8559.
40 H. A. Faizi, S. L. Frey, J. Steinkühler, R. Dimova and P. M. Vlahovska, *Soft Matter*, 2019, **15**, 6006–6013.
41 M. Adamo, A. S. Poulos, R. M. Miller, C. G. Lopez, A. Martel, L. Porcar and J. T. Cabral, *Lab Chip*, 2017, **17**, 1559–1569.
42 M. Adamo, A. S. Poulos, C. G. Lopez, A. Martel, L. Porcar and J. T. Cabral, *Soft Matter*, 2018, **14**, 1759–1770.
43 Y. Son, *Polymer*, 2007, **48**, 632–637.
44 H. P. Martin, PhD thesis, Imperial College London, 2010.
45 S. Förster, A. Timmann, C. Schellbach, A. Frömsdorf, A. Kornowski, H. Weller, S. V. Roth and P. Lindner, *Nat. Mater.*, 2007, **6**, 888–893.
46 I. W. Hamley, *Introduction to Soft Matter: Synthetic and Biological Self-Assembling Materials*, 2007, pp. 1–328.
47 R. Hołyst, *Phys. Rev. A: At., Mol., Opt. Phys.*, 1991, **44**, 3692–3709.
48 L. Gentile, C. Oliviero Rossi and U. Olsson, *J. Colloid Interface Sci.*, 2012, **367**, 537–539.
49 F. Nettesheim, J. Zipfel, U. Olsson, F. Renth, P. Lindner and W. Richtering, *Langmuir*, 2003, **19**, 3603–3618.
50 L. Gentile, M. A. Behrens, L. Porcar, P. Butler, N. J. Wagner and U. Olsson, *Langmuir*, 2014, **30**, 8316–8325.
51 A. S. Wunenburger, A. Colin, T. Colin and D. Roux, *Eur. Phys. J. E: Soft Matter Biol. Phys.*, 2000, **2**, 277–283.